Semiconductor Science and Technology

TOPICAL REVIEW

Optically pumped nanowire lasers: invited review

Semicond. Sci. Technol. **25** (2010) 024001 (12pp) doi:10.1088/0268-1242/25/2/024001

TOPICAL REVIEW

Optically pumped nanowire lasers: invited review

Mariano A Zimmler[1], Federico Capasso[1], Sven Müller[2] and Carsten Ronning[3]

[1] School of Engineering and Applied Sciences, Harvard University, Cambridge, MA 02138, USA
[2] II Institute of Physics, University of Göttingen, 37077 Göttingen, Germany
[3] Institute for Solid State Physics, University of Jena, 00743 Jena, Germany

E-mail: capasso@seas.harvard.edu

Received 27 April 2009
Published 22 January 2010
Online at stacks.iop.org/SST/25/024001

Abstract
This paper reviews several topics related to optically pumped ZnO nanowire lasers. A systematic study of the various properties of a device as it evolves from the regime of amplified spontaneous emission to laser oscillation above threshold is presented. The key dependence of the laser threshold on nanowire diameter is demonstrated and explained by means of a thorough study of guided modes in semiconducting nanowires for a nanowire-on-substrate geometry. A 'head on' detection geometry is used to measure the far-field profile of a nanowire laser and thus identify the modes responsible for lasing. Finally, the temperature behavior of a nanowire laser is reported, and possible mechanisms that may be responsible for gain are suggested.

(Some figures in this article are in colour only in the electronic version)

1. Introduction

The possibility of laser action in semiconductor nanowires is nothing short of intriguing. Such devices could potentially generate highly localized intense monochromatic light in a geometry ideally suited for the efficient coupling into nanophotonic elements such as quantum dots, metallic nanoparticles, plasmonic waveguides and even biological specimens. Thus, nanowire lasers could become a critical component in the study and development of novel nanoscale photonic elements. The research community has consequently extended significant efforts toward their realization, but most studies have succeeded only in providing evidence of amplified spontaneous emission (ASE) [1–8]. While more recent work on gallium antimonide (GaSb) nanowires [9] shows some evidence of lasing, the conclusive demonstration of laser oscillation has remained elusive. In particular, most works have failed to observe a laser threshold marking the transition between a superlinear region, characteristic of ASE, and a *linear* region, characteristic of laser oscillation, with increasing pump power or drive current [10]. Furthermore, the study of individual nanowires has usually been conducted in an epifluorescence setup. In such a configuration, a single microscope objective is used for excitation and collection, so that only light scattered at 90° from the nanowire axis can be collected, preventing a full characterization of the angular and polarization dependence of the laser emission.

Recently, we reported direct evidence of laser action in optically pumped nanowires [11]. In that work, we successfully observed the transition from ASE to laser oscillation in ZnO nanowires at room temperature. Furthermore, we introduced a 'head on' detection configuration that permitted the first accurate measurement of the power emitted by a single nanowire.

In this paper, we review our previous work and present, in addition, a complete study of the mode structure of nanowires in a nanowire-on-substrate geometry. We also extend our head on detection results to include the first measurement of the far-field profile of a single nanowire. Finally, we also present results on the temperature behavior of our devices.

Laser oscillation occurs when the cavity round-trip gain equals the round-trip losses [10], which in nanowires are typically dominated by the mirror losses (that is, transmission at the end facets). This is the result of diffraction: when the

diameter of the nanowire is comparable to or smaller than the wavelength of light in the semiconductor, the optical field can extend considerably outside the nanowire. This contributes to the mirror losses because only the fraction of the field that is confined inside the nanowire experiences a refractive index contrast at the end facets, therefore limiting the amount of reflection and feedback. Thus, it would appear that we are faced with a fundamental trade-off: while narrow-diameter nanowires satisfy our need for compactness, they present large losses which might prevent lasing. We will explore this relationship below.

This paper is structured as follows. We begin with a presentation of *unambiguous* evidence of optically pumped laser action in ZnO nanowires, which is supported by the observation of a clear transition between ASE and laser oscillation. By systematically studying nanowires of different dimensions, we then demonstrate the existence of a critical diameter below which no lasing occurs. In order to understand such behavior quantitatively, we next solve for the dispersion properties of a ZnO nanowire on a silica substrate and compute the facet reflectivity for a few of the lowest-order guided modes. Armed with these tools, we estimate diameter and length dependence of the threshold gain for our nanowires and compare this to our experimental findings. Next, we introduce an alternative 'head on' detection geometry, with which we measure the far-field profile of a single nanowire laser and thus identify the oscillating modes. Finally, we present a cursory examination of the temperature dependence of lasing in these devices and suggest possible gain mechanisms which may be at work.

2. Synthesis

The ZnO nanowires used in this work were synthesized with a VLS technique [12]. The distinguishing feature of the process presented here is the use of *pure ZnO powder*, rather than a combination of ZnO and graphite, as the source material. The powder was placed in an alumina boat at the center of a horizontal tube furnace and heated up to 1350 °C, at a rate of 190 °C h^{-1}, and kept at this temperature for the duration of the growth (30 min). The resulting ZnO vapor was transported with argon gas (50 sccm flow rate at a system pressure between 100 and 200 mbar) to a position in the furnace where the temperature ranged between 960 and 1150 °C, and where it condensed to form nanowires on an Au-covered (with a 4 nm thick film) silicon substrate. Only during the growth at 1350 °C was the argon flow direction set to transport the ZnO vapor from the source to the substrate. During the heating-up and cooling-down phases the gas flow direction was reversed. A growth duration of 30 min results in a dense sample of randomly arranged ZnO nanowires, as shown in the SEM image in the inset of figure 1. The nanowires exhibit a broad diameter distribution between 100 and 400 nm and lengths up to 100 μm.

3. Structural characterization

Figure 1 shows a representative Θ–2Θ x-ray diffraction (XRD) spectrum (taken with a D8 Discover Bruker AXS spectrometer

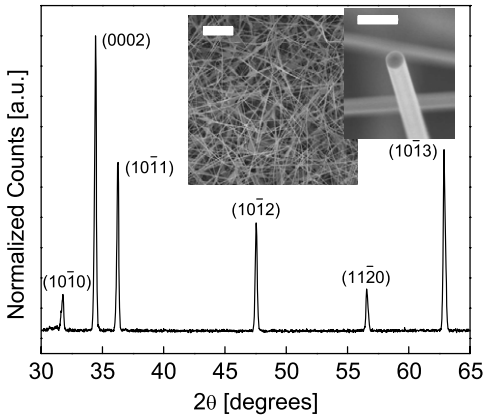

Figure 1. Representative x-diffraction spectrum of an as-grown ZnO nanowire ensemble sample. Inset (left): SEM micrograph of the as-grown ensemble of ZnO nanowires on the growth substrate. The scale bar is 10 μm. Inset (right): SEM micrograph of a single ZnO nanowire. The scale bar is 500 nm.

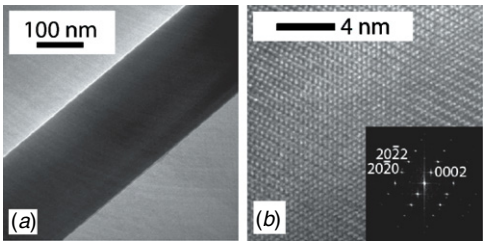

Figure 2. (*a*) Bright-field and (*b*) high-resolution TEM micrographs of an individual ZnO nanowire. Inset: FFT analysis of (*b*).

using 0.154 nm CuKα radiation) of a ZnO nanowire ensemble sample. The diffraction peaks are clearly visible and can all be indexed to the hexagonal ZnO lattice with constants $a = 0.325$ nm and $c = 0.521$ nm (Joint Committee on Powder Diffraction Standards (JCPDS), file no 36–1451). No characteristic lines from Zn or other alloys were detected.

The microstructure of individual ZnO nanowires was characterized by high-resolution transmission electron microscopy (HRTEM) (using a Philips CM 200-FEG-UT TEM, with the nanowires dispersed on carbon-coated TEM grids). Figure 2(*a*) shows a typical low-resolution bright field image of a nanowire which exhibits uniform contrast over its entire length and, therefore, together with figure 1, strongly suggests that the nanowires are single crystals. Lattice and structural defects, such as stacking faults, twins or dislocations, would typically result in clear contrast variations in such a bright field image. Furthermore, while an amorphous structure would also result in an image with uniform contrast, figure 1 suggests our material is indeed crystalline. Figure 2(*b*) shows a high-resolution TEM micrograph of a small section of a nanowire, but representative of the whole structure, which highlights the regular and periodic ZnO crystal without any structural defects, metal catalysts or amorphous regions. A Fourier transform (FFT) analysis of figure 2(*b*) is shown in the inset and reveals the hexagonal lattice structure with the respective lattice constants. For example, the distance from the central spot to the 0002 peak is ≈3.99 nm^{-1}, which corresponds to a lattice distance of 0.25(± 5%) nm, in good agreement with the expected value of 0.2603 nm. Furthermore,

we can clearly see from the TEM analysis that the ZnO nanowires grow, in general, in the *c*-axis direction, which is in agreement with the literature [13].

4. Amplified spontaneous emission and laser oscillation

After growth, the nanowires were dispersed onto a Si/SiO_2 substrate (with a 500 nm thick thermal oxide) for optical characterization. Individual nanowires were pumped with the frequency-tripled output (355 nm) of a Nd:YAG laser (500 Hz, 6 ns pulse length), focused to a diameter of ∼100 μm, using a reflective microscope objective. The excitation intensity was attenuated by changing the Q-switch delay of our pump laser together with the use of neutral density filters. Their emission was collected with the same objective. All measurements were performed at room temperature, unless otherwise noted. While limited in its utility for the study of the angular and polarization dependence of the facet emission, this configuration enables us to study a large number of nanowires of varying lengths and diameters, which is necessary to elucidate the threshold dependence on nanowire dimensions.

Figures 3(*a*) and (*b*) show the luminescence spectra and the corresponding CCD images, respectively, for a ZnO nanowire as a function of pump intensity I_{ex}. For $I_{ex} \lesssim 200$ kW cm^{-2}, the spectra are broad and featureless, centered around ∼382 nm and with a full-width at half-maximum (FWHM) of 19.3 nm. In this regime, light is emitted essentially isotropically along the nanowire—as seen in the second panel from the bottom of figure 3(*b*)—and the output power (shown in figures 3(*c*) and (*d*)) depends *linearly* on the excitation intensity, consistent with spontaneous emission. For 200 kW cm$^{-2} \lesssim I_{ex} \lesssim 300$ kW cm^{-2}, the spectra consist of a broad emission with the addition of sharp (FWHM < 0.4 nm) emission lines. In this regime, population inversion starts building up, leading to ASE along the nanowire at wavelengths corresponding to the longitudinal modes (see section 5) and thus to enhanced emission from the nanowire ends. Furthermore, the output power exhibits a *superlinear* increase with pump intensity, which is the expected behavior as the laser threshold is approached [10, 14]. For $I_{ex} \gtrsim 300$ kW cm^{-2}, the spectra are dominated by sharp emission lines: their intensity is orders of magnitude greater than the spontaneous emission background. The output power depends *linearly* on excitation intensity and is concentrated in a narrow emission range (385 nm < λ < 390 nm). Figure 3(*c*) also shows a fit (solid line) with a multimode laser model [14], which gives a threshold of ≃270 kW cm^{-2}. The theory in [14] gives the output power of the laser as a function of the normalized pump rate and a parameter x_0, which is proportional to the mode density (see equation (23)). An excellent fit of this equation to the data is obtained with $x_0 = 0.016$. Figure 3(*d*) shows the same data and fit as figure 3(*c*) on a log–log scale. Note that the threshold in semiconductor lasers is 'softer' than in other lasers due to the small cavity volume and the relatively high levels of spontaneous emission [10, 14]. In summary, the data of figure 3 show the expected behavior of the output power of the nanowire device as it passes through the threshold for laser oscillation.

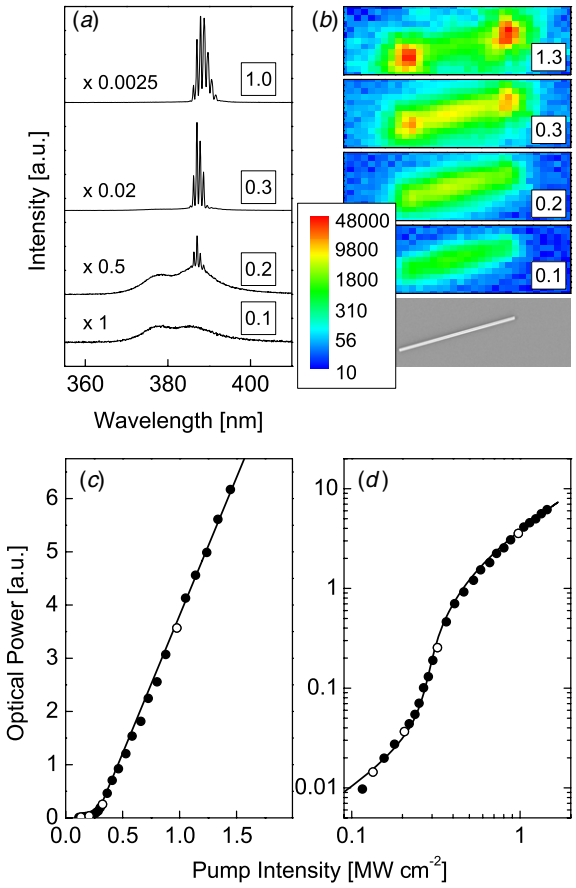

Figure 3. Laser oscillation in ZnO nanowires. (*a*) Output spectra versus pump intensity of a 12.2 μm long 250 nm diameter ZnO nanowire. (*b*) SEM image and CCD images, under different pump intensities, for the same nanowire as in (*a*). The labels indicate the pump intensity in units of MW cm^{-2}. The color scale indicates the number of counts. (*c*) Pump intensity dependence of the total output power (circles) for the same nanowire. The solid line is a fit to the data using the model in [14]. The optical power was collected from the scattered light at one of the nanowire ends. (*d*) The same data and fit on a log–log scale. The open circles correspond to the spectra shown in (*a*).

5. Fabry–Pérot waveguide modes

The sharp features observed in figure 3(*a*) correspond to longitudinal Fabry–Pérot waveguide modes. The mode spacing in a Fabry–Pérot cavity is given by [10]

$$\Delta\lambda = \frac{1}{L}\left[\frac{\lambda^2}{2}\left(n - \lambda\frac{\mathrm{d}n}{\mathrm{d}\lambda}\right)^{-1}\right], \qquad (1)$$

where L is the cavity length, and n is the index of refraction at wavelength λ. Thus, for a fixed λ, the mode spacing Δλ should scale in proportion to the inverse length $1/L$. This behavior is illustrated in figure 4(*b*), which shows *above-threshold* spectra for nanowires of different lengths and a plot of Δλ for nine nanowires. The slope of the fit is 10 765(±1.7%) nm^2. With $\lambda = 385$ nm and $n = 2.4$, this gives $\mathrm{d}n/\mathrm{d}\lambda \approx -0.012$ nm^{-1}. This value is in reasonable agreement with published data for ZnO [15], which gives $\mathrm{d}n/\mathrm{d}\lambda \approx -0.015$ nm^{-1}.

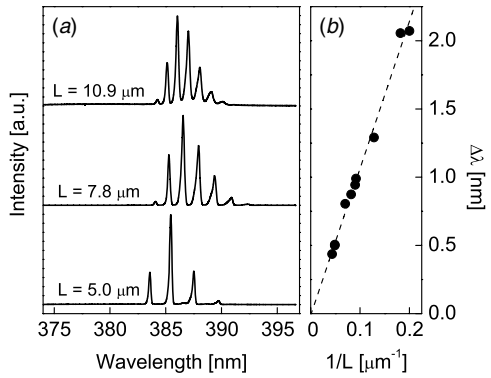

Figure 4. Nanowire length dependence of *above-threshold* laser spectra for ZnO nanowires. (*a*) Laser oscillation spectra for three nanowires of different lengths. (*b*) Spacing between adjacent modes versus $1/L$. Note that the linear fit extrapolates to 0 nm spacing for $L \to \infty$.

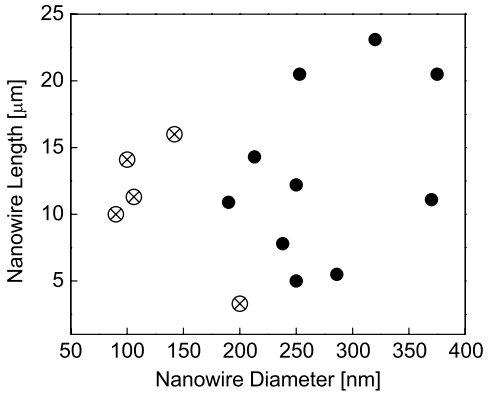

Figure 5. Experimental results on lasing for nanowires of different dimensions: crosses (⊗) indicate nanowires which did not lase, and circles (●) indicate those which did.

6. The role of nanowire dimensions

The threshold condition for laser oscillation is that the round-trip gain inside the nanowire must equal the round-trip losses [10]:

$$\Gamma g_{\text{th}} = \alpha_{\text{w}} + \alpha_{\text{m}}, \tag{2}$$

where Γ is the confinement factor, g_{th} is the material gain, α_{w} is the waveguide loss, and α_{m} accounts for the losses at the end facets (i.e. the mirror losses):

$$\alpha_{\text{m}} = \frac{1}{L} \ln \frac{1}{R}. \tag{3}$$

Here L is the length of the nanowire, and R is the power reflectivity. In contrast to conventional edge emitting semiconductor lasers where typically $\alpha_{\text{w}} > \alpha_{\text{m}}$, in nanowire lasers $\alpha_{\text{m}} \gg \alpha_{\text{w}}$ due to the much smaller cavity length and the smaller reflection coefficient [16]. As a result, the threshold gain is a strong function of L and the nanowire diameter D. Figure 5 shows the devices that lased and those which did not (the former ones indicated by filled circles) in the plane defined by the two key dimensions: diameter and wire length. Nanowires with diameters smaller than ∼150 nm did not reach threshold, independent of the nanowire length up to a value of 16 μm (that is, within the parameter space we studied). Qualitatively, this can be explained by the diameter dependence of the reflection coefficient R, which is directly related to the confinement factor Γ [16], as was explained in the introduction. For example, for the most confined mode in our geometry, the fraction of the mode intensity inside the nanowire decreases from ∼85% for $D = 150$ nm to <1% for $D = 100$ nm. In order to understand these results quantitatively, however, we need to perform a full numerical calculation, which we present in the following.

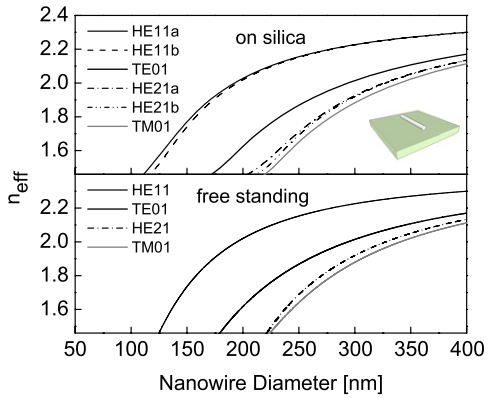

Figure 6. Normalized propagation constant $n_{\text{eff}} = k_z c/\omega$ as a function of nanowire diameter D for a few of the lowest-order modes of (top) a nanowire lying on a silica substrate and (bottom) the cylindrically symmetric case of a free-standing nanowire surrounded by air. The calculation was done with a commercial software package. Here we take the index of refraction of ZnO to be 2.4 (at 385 nm) and that of SiO_2 to be 1.46. For ease of comparison to the case of a nanowire on silica, the calculation for a free-standing nanowire is only shown in the range $1.46 \leqslant n_{\text{eff}} \leqslant 2.4$. Note also that the HE$_{nm}$ modes, which are degenerate in a free-standing nanowire, split when the nanowire is placed on a silica substrate. The two possibilities are labeled as HEmna and HEmnb.

7. Reflection of guided modes

As we have seen in previous sections, nanowires appear to support guided modes that propagate along their axes. Accurate estimates of the threshold gain of these structures therefore demand knowledge of the field distributions of those modes as well as their reflectivity off the nanowire facet. In this section, we begin by presenting the dispersion properties of nanowires lying on a silica substrate (according to our experimental configuration) and calculate the field distributions of the lowest-order guided modes, which are those most likely to be relevant for lasing. We then compute the reflectivities of these modes by solving Maxwell's equations using the finite-difference time-domain (FDTD) method (we use the commercial engine *FullWAVE*$^{\text{TM}}$, which is part of the RSoft Photonic Suite). We conclude with a calculation of the threshold gain in semiconductor nanowires and use this information to interpret the results from the previous section.

We begin with an analysis of the dispersion properties of a ZnO nanowire of diameter D lying on a SiO_2 substrate and surrounded by air, as shown schematically in the inset of figure 6. In the simplest case, a free-standing nanowire

can be modeled as a uniform dielectric cylinder[4], the analysis of which is identical to that of the well-known step-index fiber [17]: simply set the core refractive index to that of the nanowire, choose the radius of the cladding infinitely large and set its refractive index to that of air. In our experimental configuration, however, the nanowires lie on a substrate with an index of refraction greater than that of air. This not only breaks the cylindrical symmetry of the problem, rendering the calculation tractable only numerically, but also distorts the optical mode (with respect to the cylindrically symmetric case) by 'pulling' the field preferentially into the substrate.

We should emphasize that most of the experimental work on nanowires is actually carried out in such a nanowire-on-substrate geometry. This is simply a consequence of the growth process, which generally results in large numbers of overlapping nanowires (see the inset in figure 1). In order for the study of individual structures to be feasible, the nanowires need to be removed from the growth substrate and deposited onto a different clean substrate (SiO_2 and Al_2O_3 are two frequent choices) in such a way that adjacent wires are spaced far apart. While the influence of a substrate can actually be neutralized experimentally with the use of a mesoporous silica film[5], such a film would not be amenable to the processing required for, for example, electrical injection devices, so that the use of a substrate such as SiO_2 may be unavoidable in many circumstances. This makes the following study of considerable interest.

A ZnO nanowire on a SiO_2 substrate can support modes that closely resemble the transverse electric (TE_{0m}), transverse magnetic (TM_{0m}) and hybrid (HE_{nm} and EH_{nm}) modes typically found in the cylindrically symmetric case of a free-standing nanowire [16]. Figure 6 shows the dependence of the normalized propagation constant $k_z c/\omega$ (also known as the effective mode refractive index) on the nanowire diameter, where k_z is the wave vector along the nanowire axis, ω is the frequency, and c is the speed of light in vacuum. As suggested by physical intuition, the departure from the cylindrically symmetric, air-clad case, is greatest for diameters for which the mode is poorly confined to the nanowire. In those cases, the field extends for a considerable distance beyond the surface, and is therefore influenced by the presence of the substrate, which has a greater index of refraction than air. Note, however, that for slightly larger diameters the mode becomes quickly confined in the transverse direction, making the presence of the substrate irrelevant. As we would expect, for large nanowire diameters the mode is well confined, and the system converges to the cylindrically symmetric case. Two other points are worth noting. First, the HE_{11} mode exhibits a cutoff, unlike the cylindrically symmetric case. Second, the HE_{mn} modes, which are degenerate in the cylindrically symmetric case (they can have either a $\cos n\phi$ or $\sin n\phi$ dependence), are now split, with one mode extending more into the substrate (labeled as HE*mn*a in figure 6) and the other extending more into air (labeled as HE*mn*b in figure 6).

[4] High-resolution SEM images show that our nanowires are not strongly faceted, so that this is indeed an excellent approximation. See, for example, the inset in figure 1.

[5] Such a film can have an index of refraction close to that of air throughout the visible spectral region [18].

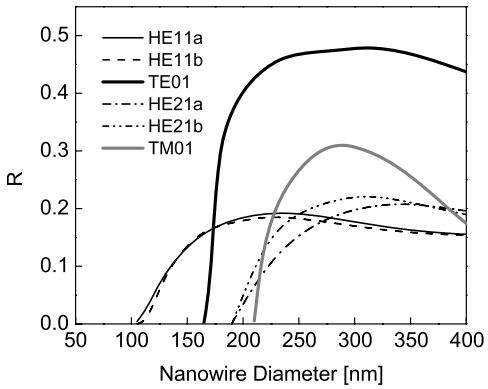

Figure 7. Reflection coefficient for a few of the lowest-order modes of a ZnO nanowire lying on a silica substrate.

We now turn to the calculation of the reflection coefficient for guided modes. The numerical approach is based on solving Maxwell's equations using the FDTD method [19] in three dimensions, and is an extension of the same calculation for a free-standing nanowire [16]. The size of the computational domain is 1 μm in the x- and y-directions (perpendicular to the nanowire axis) and 5 μm in the z-direction (along the nanowire axis). With a grid size of $\lambda/20n \approx 8$ nm in all directions, this corresponds to $\sim$120 points in the x- and y-directions and $\sim$620 points in the z-direction. We also surround the computational domain with a perfectly absorbing layer to prevent unwanted reflections. To obtain the reflection coefficient we proceed as follows. First, we solve for the spatial distribution of all six field components of the guided mode we are interested in. Using a field source inside the nanowire we can then excite this mode (using continuous wave excitation with a free space wavelength of 385 nm), which propagates from the launch point toward the end of the wire. This is the forward wave. Upon incidence on the facet, some of the radiation couples into the far field and some of it is reflected back. This is the backward wave. Only when the system has reached steady state, after a long enough simulation time, we calculate the reflection coefficient as the ratio of the intensity of the backward to the forward wave. We should emphasize that upon incidence on the nanowire facet several different modes can be excited that propagate backward: these include all guided modes with the same frequency and azimuthal dependence as the incident mode [16]. Our calculation of the reflection coefficient, therefore, includes *only* the component which couples into itself, which is the one relevant for feedback considerations:

$$R(t) = \frac{\int (\Phi_r \cdot \Phi_0^*)\, \mathrm{d}A}{\int (\Phi_f \cdot \Phi_0^*)\, \mathrm{d}A}, \tag{4}$$

where Φ_r is the backward wave, Φ_f is the forward wave, Φ_0 is the mode profile of the guided mode, and the integrals are taken over a cross section. The reflection coefficient is obtained as the time average of equation (4). Figure 7 shows the reflection coefficient for different guided modes as a function of nanowire diameter. As we can see, when the diameter is roughly less than 170 nm, only the HE_{11} mode exists and it exhibits very low reflectivity ($R \lesssim 15\%$). For nanowires with

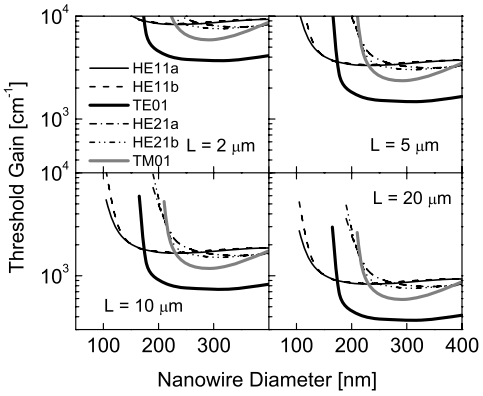

Figure 8. Threshold gain, as given by equation (2), for a ZnO nanowire lying on a silica substrate, with the assumption that $\alpha_m \gg \alpha_w$, as a function of nanowire diameter and for several nanowire lengths.

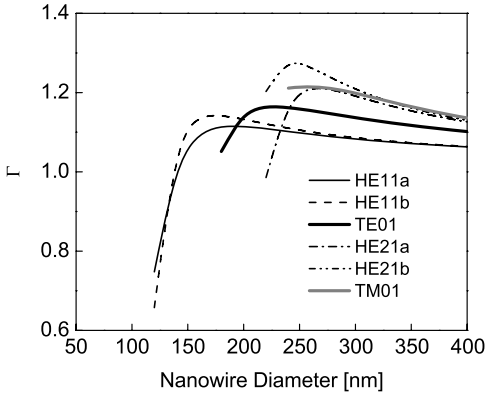

Figure 9. Confinement factor for a few of the lowest-order modes of a ZnO nanowire lying on a silica substrate.

diameters larger than 170 nm, on the other hand, several other modes are possible. Of these, the TE_{01} mode exhibits the largest reflectivity, $R \approx 47\%$, almost as soon as the mode is allowed, which is more than twice the reflectivity of the HE_{11} mode, and roughly 50% larger than the maximum value for the TM_{01} mode. In figure 8, we have used the results of the reflectivity calculation for the various modes, in conjunction with equations (2) and (3), to calculate the threshold gain for nanowires of various dimensions. Figure 8 reinforces the conclusions reached from the reflectivity data. For nanowires with $D \gtrsim 170$ nm, the TE_{01} mode clearly exhibits the lowest thresholds, which can be up to one order of magnitude lower than the threshold for nanowires with $D < 150$ nm (for the same nanowire length), for which only the HE_{11} mode exists. For nanowires with $D \gtrsim 200$ nm, the TM_{01} mode is also possible and it exhibits the next higher thresholds, which are approximately 50% larger than those corresponding to the TE_{01} mode. These results suggest that the TE_{01} and TM_{01} modes are the most likely to lase for nanowires with diameters larger than 170 nm, whereas when $D < 170$ nm, if lasing is at all possible given the sharp increase in the threshold, nanowires would lase in the HE_{11} mode.

8. Mode confinement

As we have explained above, the threshold condition for laser oscillation is given by $\Gamma g_{th} = \alpha_w + \alpha_m$. The expression, Γg_{th}, is commonly referred to as the modal gain, i.e. the percentage power increase *per unit length along the propagation direction* gained by the waveguide mode from the active region. The confinement factor Γ is usually taken to mean the fraction of the optical mode intensity contained within the active region [20]. This, however, is not entirely accurate for semiconductor nanowires[6]. The modal gain is, in fact, defined as the growth rate of power in the waveguide by means of the expression

$$\frac{dP(z)}{dz} = \Gamma g P(z). \tag{5}$$

[6] We thank Professor Cun-Zheng Ning for bringing this to our attention. See [21] for a full discussion.

Here $P(z)$ is the power as a function of distance along the waveguide, and g stands for the material gain (we assume isotropic gain for simplicity). The confinement factor is then given by [21]

$$\Gamma = \frac{c\sqrt{\epsilon}}{2\pi P_0} \int_{nw} |\mathbf{E}|^2 \, dA, \tag{6}$$

where ϵ is the dielectric constant of the nanowire, and $\mathbf{E}$ is the complex electric field. The integral is over a nanowire cross section, and P_0 is given by

$$P_0 = \int (\mathbf{S} + \mathbf{S}^*)\hat{\mathbf{z}} \, dA, \mathbf{S} = \frac{c}{4\pi} \mathbf{E} \times \mathbf{H}^*, \tag{7}$$

with $\mathbf{S}$ being the Poynting vector (i.e. P_0 is an integral of the time averaged energy flux over an infinite plane perpendicular to the direction of propagation). Thus, the confinement factor can be calculated directly from the field distributions. In the limiting case of weak waveguiding [21], the confinement factor becomes the ratio of the power inside the nanowire to the total power, as is usually assumed in the literature. However, for strong waveguiding, the confinement factor can exceed unity. As discussed in [21], this phenomenon can be understood physically by noting that, in a planar waveguide, a guided wave can be represented as a plane wave that propagates at some angle with respect to the z-direction, and therefore experiences multiple reflections at the waveguide boundaries. The total distanced traveled by this wave is larger than for a plane wave propagating along the z-direction, so that the gain per unit distance along the z-direction can be larger if the wave is well confined to the active region. Figure 9 shows the confinement factors for a ZnO nanowire lying on a silica substrate, calculated according to equation (6).

9. 'Head on' measurements

As we have seen in the last two sections, a ZnO semiconductor nanowire can theoretically support several optical modes exhibiting different dispersion, polarization, field distributions and losses. Naturally, a complete study of a nanowire laser demands that we determine which of these modes actually occurs in practice and under what conditions. This can be done with a full characterization of the far-field emission that

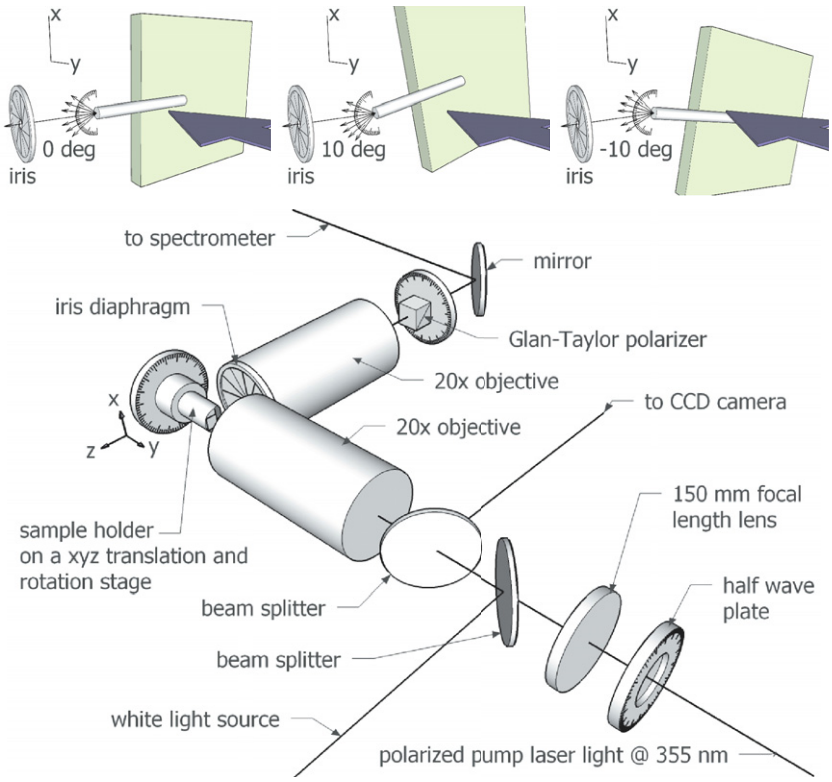

Figure 10. Experimental setup for the measurement of the far-field emission of a semiconductor nanowire. Note that the angle between the nanowire axis and the emission selected by the iris diaphragm is what we refer to as θ in what follows. The x-axis is aligned with the plane of the substrate and the y-axis is perpendicular to it.

originates at the nanowire end facets [22]. However, as we have mentioned in the introduction, the detection geometry we have used so far is not well suited for this purpose. Such an undertaking requires an alternate experimental configuration, where the nanowire emission can be collected 'head on'. Figure 10 shows a setup designed to do this. The top panels show a detail of the sample: a nanowire is shown partially suspended in air and partially resting on a silica substrate. This is needed for the end emission to be collected without any scattering from the substrate. The nanowire is then optically pumped uniformly along its length, and the emission is collected from one end, at an angle of 90° from the excitation beam. By rotating the sample stage about the position of the nanowire, in the xz plane, in conjunction with the use of an iris diaphragm on the collection objective, we can thus achieve angular resolution. The polarization information can then be obtained with a Glan–Taylor polarizer placed immediately after the collection objective. The bottom panel shows the optical setup. Note that in this configuration it is necessary to rotate the polarization of the exciting laser by the same amount as the nanowire, which justifies the insertion of a half wave plate in the path of the excitation beam. The reason for this is that semiconductor nanowires exhibit polarization anisotropy: given the same excitation intensity, the photoluminescence intensity emitted by a nanowire is largest when the polarization of the optical pump is aligned with the nanowire axis[7]. The lens in front of the half wave plate is placed at a distance larger than twice its focal length from the microscope objective and is therefore used to *expand* the pump laser beam, which is needed in order to excite the entire length of our nanowires uniformly. The combination of two beam splitters in the path of the pump laser, which introduce white light illumination and redirect the image collected by the objective into a CCD camera connected to a TV, is used to locate the nanowire and to align it with the excitation spot.

Before we proceed with the discussion of the angular and polarization dependence of the far-field emission of a nanowire, we should note that the 'head on' geometry we have just introduced can be used to perform an accurate measurement of the output power of a semiconductor nanowire laser. This is accomplished by removing the iris diaphragm and replacing the Glan–Taylor polarizer with a single-channel silicon detector (we use the module UVS-025-H, manufactured by Electro-Optical Systems Inc., which is a room-temperature silicon receiver optimized for UV operation). Figure 11 shows the detected peak power versus pump peak power for a 17 μm long 244 nm diameter ZnO nanowire. The slight flattening of the slope of the curve for pump power close to 40 mW could be due to a heating

[7] While the exact calculation depends on the nanowire diameter and the excitation wavelength, and therefore requires a full electrodynamical treatment, we can offer a simple estimate for an infinite dielectric cylinder in a constant external field **E**. In that case, the ratio between the emission intensity when the excitation polarization is perpendicular to the cylinder's axis to the intensity for parallel polarization is $[2\epsilon_0/(\epsilon + \epsilon_0)]^2$, where ϵ_0 is the dielectric constant of vacuum, and ϵ is the dielectric constant of the cylinder [23]. Physically, this is just a result of the continuity of the transverse component of the displacement field in Maxwell's equations.

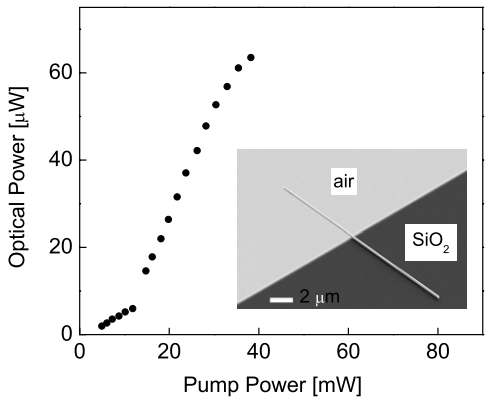

Figure 11. Peak optical power, uncorrected for the collection efficiency (10%), measured 'head on' at the nanowire end.

effect. The inset shows an SEM image of the sample (compare with the top panel in figure 10). While we presently lack a robust method to prepare these samples, we have found that by first depositing nanowires onto a Si/SiO_2 substrate and then cleaving it into several smaller pieces typically results in a few partially suspended nanowires.

The theoretical polarization and angular distribution of the intensity of the first three lowest-order modes of a free-standing nanowire (HE_{11}, TE_{01} and TM_{01}) have already been studied in great detail in [22]. Here we will only summarize the results. The emission of the HE_{11} mode is characterized by a maximum around $\theta = 0^\circ$. With increasing nanowire diameter, the forward intensity (that is, the emission for $\theta = 0^\circ$) decreases and the backward intensity (that is, the emission for $\theta > 90^\circ$) increases. We should note, however, that in our experimental configuration it is not possible to distinguish between the forward emission of one facet and the backward emission of the other facet. This mode is also dependent on the azimuthal angle. In contrast, the distinguishing feature of the TE_{01} and TM_{01} modes is the absence of emission at $\theta = 0^\circ$, which is a consequence of the symmetry of the modes. Furthermore, the maxima of the intensities lie in the region 30°–50°. While both the modes exhibit cylindrical symmetry (that is, they are independent of the azimuthal angle), the TE_{01} mode is polarized azimuthally whereas the TM_{01} mode is polarized radially.

Figure 12 shows our experimental results for a 10 μm long 200 nm diameter nanowire, together with the results of FDTD simulations for our proposed mode assignment. It is important to emphasize that these measurements correspond to the far-field profile in the plane of the substrate (as indicated by the dotted line in the inset of figure 12(*b*)) and are not necessarily cylindrically symmetric. Figure 12(*a*) shows the emission intensity for light polarized in the y-direction, which corresponds to azimuthal polarization, whereas figure 12(*b*) shows the intensity recorded for light polarized in the x-direction, which corresponds to radial polarization. *As we can see, both polarizations exhibit negligible emission for* $\theta = 0^\circ$. Based on the previous discussion of the work by [22], our data seem to point to the TE_{01} and TM_{01} modes as candidates for assignment. The dashed line in figure 12(*a*) shows the theoretically predicted intensity distribution for a TE_{01} mode, which is also polarized in the y-direction for this geometry. Similarly, the dashed line in figure 12(*b*) shows the theoretically predicted intensity distribution for a TM_{01} mode, which is polarized in the x-direction. Several comments are in order. While the agreement between the measured and simulated profiles appears to be generally good for this particular device, other nanowires exhibited far-field intensity distributions with strong asymmetry about the $\theta = 0^\circ$ direction (in fact, even for the device shown in figure 12 there is a slight asymmetry in the profile for light polarized in the x-direction). The origin of these deviations is unclear at present but we can offer a number of hypotheses. First, FDTD simulations suggest that the exact geometry of the end facet strongly influences the far field of the mode. For example, the far field of the TE_{01} mode in a nanowire with a rounded end facet (that is, where the end facet is a hemisphere with a radius of curvature equal to that of the nanowire)

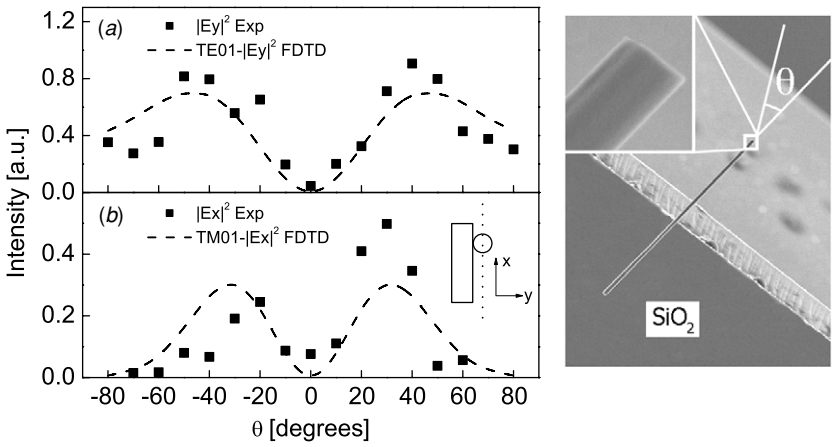

Figure 12. Far-field intensity of a 10 μm long 200 nm diameter ZnO nanowire as a function of θ for light polarized in (*a*) the y- and (*b*) x-directions. Both profiles were measured with a pump peak power of ∼10 mW. The lines show the theoretically predicted intensities for (*a*) a TE_{01} and (*b*) a TM_{01} mode. The inset in (*b*) shows a schematic cross section of a device, and the dotted line indicates the plane on which the far-field measurement is taken. The image on the right is an SEM image of the partially suspended nanowire and the inset shows a detail of the end facet.

exhibits a maximum around ∼75° (rather than ∼45° for a flat facet). Thus, whether the end facet is rounded or not, whether the normal to the facet is at an angle (different from 0°) from the nanowire axis, and even surface roughness, could all potentially contribute to produce a far-field profile which deviates from the prediction for the perfectly flat circular case. Second, it is also conceivable that the substrate, albeit unimportant for thick nanowires with well-confined low-order modes, can have an effect on the nanowire far field. For example, a mode traveling along the nanowire in the direction toward the substrate will scatter and partially reflect once it reaches the substrate edge. Thus, if the nanowire axis is at an angle different from 90° from the substrate edge, this might result in a far-field profile that is still symmetric with respect to the substrate edge but not the nanowire axis.

10. Temperature dependence

We devote this final section to a discussion of the physical mechanisms that could be responsible for the gain in our devices. All the experimental results presented in this section correspond to the same nanowire as in figure 3. ZnO and, more generally, II–VI compound semiconductors (such as CdS and CdSe) behave fundamentally in a different way from III–V semiconductors, which are typically used for injection lasers. In III–V materials, the optical transitions that can be used for laser action are band-to-band transitions [24]. In II–VI compounds, the recombination process of electrons and holes via exciton states is more favorable, but direct exciton recombination cannot lead to laser action because a system of an exciton coupled to a photon is equivalent to two coupled oscillators [25, 26]. The laser process in II–VI compounds thus requires the participation of a third field [27]. Three processes appear to be the most relevant:

(1) Exciton–exciton (ex–ex) scattering, which results in the emission of a photon and the simultaneous excitation of one of the excitons into the $n = 2, 3, \ldots,$ state [28].
(2) Exciton–electron (ex-e) scattering, which is similar to ex–ex recombination, with the only difference that the exciton that scatters into a higher state is replaced by a free carrier [28].
(3) Exciton–longitudinal optical (LO) phonon (ex-LO) scattering, where an exciton is annihilated through the simultaneous emission of a photon and a LO phonon [27].

In all of these cases, positive gain can result as long as the final states are not thermally populated, which is simply a restatement of the condition of population inversion in III–V materials. For example, the ex–ex process will exhibit gain if the $n = 2, 3, \ldots,$ states of the second exciton are not thermally occupied. Similarly, the gain of the ex–LO process will be positive as long as there are no thermally activated optical phonons, so that the corresponding absorption process is absent. These conditions imply that different gain mechanisms can be responsible for lasing at different temperatures (with some processes even exhibiting overlapping ranges of operation) [27–31], all of which can contribute to make the temperature behavior very complex. Furthermore, at low

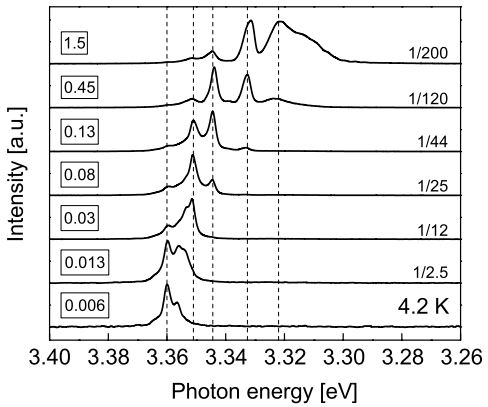

Figure 13. Output spectra versus pump intensity of a 12.2 μm long 250 nm diameter ZnO nanowire at $T = 4.2$ K (this is the same nanowire for which we have shown the room-temperature characteristics in figure 3). The boxed labels in the left indicate the pump intensity in units of MW cm^{-2} and the fractions in the right indicate the factor by which the intensity was multiplied.

temperatures ($T < 100$ K), the dominant luminescence in ZnO originates from the radiative recombination of *bound* excitons (that is, excitons bound to different crystal impurities), rather than free excitons, so that all the processes described above can *also* involve bound excitons, which give rise to different spectral signatures and power dependence [29].

Figure 13 shows the luminescence spectra as a function of pump intensity for $T = 4.2$ K. For $I_{ex} \lesssim 6$ kW cm^{-2}, the spectra are dominated by an emission line at 3.360 eV, which has generally been identified as being due to the annihilation of an exciton bound to the I_6 neutral donor [32]. As the pump intensity increases, this line quickly saturates[8] and several other lines emerge in sequence: (i) 3.356 eV, (ii) 3.354 eV, (iii) 3.351 eV, (iv) 3.344 eV, (v) 3.333 eV and (vi) 3.322 eV.[9] Lines (iii–vi) exhibit evidence of stimulated emission, which we identify by an abrupt change in the slope of the output power-versus-pump intensity curve when plotted in double-logarithmic axes (see figure 3(*d*)). We should note that some of these processes already exhibit a superlinear increase in the spontaneous emission regime[10] [31–33], so that only slopes considerably larger than two (in a log–log plot) can be indicative of stimulated emission. Two important factors, however, prevent a conclusive determination as we did in figure 3. First, a fully accurate measurement of the intensity dependence of the output power, as we did in figure 3, is not possible due to the strong overlap of the various emission lines. Unlike the room-temperature case, each line here corresponds to a different physical process, so that its intensity dependence needs to be calculated separately by integrating the number of counts within the linewidth. Second, the observation of Fabry–Pérot modes, which are indicative of feedback, is very difficult. With decreasing temperature the dominant spectral features of our devices shift to shorter wavelengths, where

[8] Saturation of this line is likely a result of almost all of the I_6 neutral donors binding an exciton [32].
[9] Note that these lines *do not* correspond to Fabry–Pérot cavity modes. We discuss this in detail below.
[10] This is the case for 'quadratic' recombination processes, such as ex–ex and ex–e, in contrast to the linear process ex–LO [31].

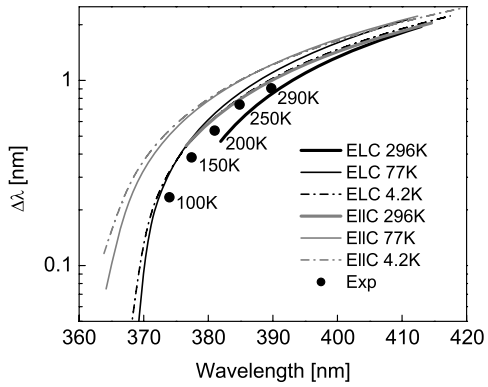

Figure 14. Temperature dependence of the Fabry–Pérot mode spacing. The lines are plots of equation (1) for the electric field oriented perpendicular (E⊥C) and parallel (E∥C) to the crystal *c*-axis. The values for *n* were obtained from [34]. The filled circles correspond to the mode spacing obtained from measured spectra, as shown in figure 3(*a*).

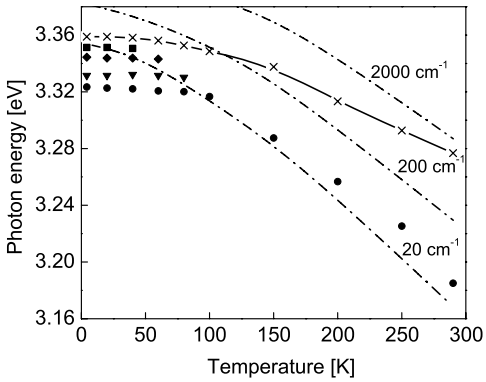

Figure 15. Temperature dependence of the peak energies of spontaneous (×) and stimulated (●) emission of a 12.2 μm long 250 nm diameter ZnO nanowire (this is the same nanowire for which we have shown the room temperature characteristics in figure 3 and the $T = 4$ K spectra in figure 13). The dash-dotted lines were taken from [39] and correspond to the photon energy values at which absorption in ZnO stays constant and given by the labels (20 cm^{-1}, 200 cm^{-1}, 2000 cm^{-1}). The other filled symbols for $T > 100$ K correspond the various stimulated emission lines observed in figure 13.

the index of refraction of ZnO increases sharply [34]. The practical consequence of this is that the Fabry–Pérot cavity mode spacing decreases and quickly falls below the resolution of our apparatus, which is ∼0.2 nm. This is shown in figure 14, where we plot the calculated cavity mode spacing, as given by equation (1), as well as the experimentally observed values for 100 K $< T <$ 290 K. When $T <$ 100 K, the luminescence concentrates in the range 369 nm $< \lambda <$ 372 nm, where the mode spacing is below our resolution (for a 12.2 μm long nanowire).

The spectra shown here are very similar to that reported for laser-excited ZnO platelets (at $T = 1.2$ K) by [32], who have interpreted these features as originating from the excited states of the I_6 donor. Such an assignment by means of the emission energy alone is, unfortunately, not unique, given that different processes can have the same energy; for example, in [29] it was reported that the emission at 3.322 eV can be due *either* to an ex–e process involving an exciton bound to a neutral donor *or* to an ex–ex collision between free excitons. In fact, a thorough review of the literature reveals that the exact emission characteristics of ZnO (and more generally II–VI semiconductors) depend on many factors including the excitation method (laser [35] or electron beam [36] irradiation), wavelength (one-photon or two-photon excitation [29]), pulse duration (longer pulses lead to heating and other effects [37]) as well as crystal quality and preparation (such as whether the sample exhibits cleaved facets or not [38]). Thus, while the exact identification of the mechanism (or mechanisms) responsible for lasing at low temperatures ($T <$ 100 K) is not possible by means of the light emission wavelength alone, *it is possible to conclude that these processes are exciton based*, since their emission energies (see figure 15) all lie >60 meV (that is, the exciton binding energy) below the bandgap of ZnO, which is ≈3.44 eV at these temperatures [15].

We can provide some more insight into the general temperature behavior of these devices for $T >$ 100 K, where the mechanism for lasing appears to be the same as at room temperature. As shown in figure 15, as the temperature increases past 100 K, the laser peak position shifts to lower energies much more rapidly than the spontaneous emission, where the latter can be related to the temperature variation of the bandgap. Note that the peak spontaneous emission energy *does not* correspond to the energy of the bandgap in ZnO, but to an energy that is smaller by ≈60 meV, which corresponds to the exciton binding energy. The rate of shift is 6.75×10^{-4} eV K^{-1}, while the spontaneous emission varies at a rate of 3.92×10^{-4} eV K^{-1}. This temperature behavior is surprising because it does not appear to coincide with the behavior predicted for any particular process. For example, if the mechanism responsible for lasing at $T >$ 100 K were the ex–LO process, as some authors have suggested [29, 31, 36], the energy position would follow the relation [29]

$$\hbar\omega = E_g(T) - E_{\mathrm{ex}} - \hbar\omega_{\mathrm{LO}} + \tfrac{3}{2}k_B T, \qquad (8)$$

where $E_g(T)$ is the bandgap energy, E_{ex} is the exciton binding energy, $\hbar\omega_{\mathrm{LO}}$ is the energy of the LO phonon, and k_B is the Boltzmann constant. However, as seen in figure 15, the peak position shifts at a rate faster than is predicted by this expression. This behavior has been observed before for ZnO platelets and has been understood as due to temperature behavior of the absorption edge of ZnO [29, 37, 40]. Figure 15 also shows the temperature dependence of the photon energy for which absorption stays constant in ZnO, where we see that the temperature variation of the laser frequency agrees very well with the position of constant absorption $\alpha = 20$ cm^{-1}. This behavior highlights an important distinction between III–V lasers operating at the bandgap energy and II–VI materials such as our ZnO devices [40]. For III–V lasers, the dominant absorption mechanism is intimately related to the gain mechanism, so that inverting the population to achieve positive gain eliminates the absorption process. In II–VI materials, where the emission mechanism is exciton mediated, gain and loss are uncoupled. As we have already discussed above, inverting the population in II–VI materials is equivalent

to the final states of the different gain processes not being thermally populated. However, band edge absorption (or other absorption mechanisms) can still contribute to the loss and, therefore, strongly influence the operation of the laser. From what we have seen, the device attempts to maintain the loss at a constant value that is much smaller than the fixed cavity losses (see figure 8).

11. Summary and conclusions

This paper has explored a wide array of topics related to laser oscillation in ZnO semiconductor nanowires by means of optical excitation. To begin, we presented *unambiguous* evidence of laser action in ZnO nanowires, at room temperature, which was supported by a systematic study of the evolution of the various device properties from ASE to laser oscillation above threshold. More importantly, we demonstrated the key dependence of the laser threshold on nanowire diameter, which we explored experimentally and justified through a thorough theoretical study of the guided modes. Furthermore, we measured the angular and polarization properties of the far-field emission from a nanowire laser. This measurement reinforced the conclusions of our theoretical study of guided modes, strongly pointing to the TE_{01} and TM_{01} modes as those responsible for lasing. Finally, we also explored the behavior of our devices at low temperatures, from room temperature to 4.2 K, which suggests that the gain mechanism is exciton mediated. This study highlights several important differences in the operation of our devices (and more generally II–VI compound semiconductors) compared to standard III–V lasers. The work presented here provides the necessary tools to obtain a basic understanding of the physics and operation of these structures as well as their optimization and possible future incorporation in photonic circuits.

Acknowledgments

We would like to thank C Borchers (University of Göttingen) for help in the TEM investigations. MAZ and FC were supported by the National Science Foundation Nanoscale Science and Engineering Center (NSEC) under contract NSF/PHY 06-46094. The support of the Center for Nanoscale Systems (CNS) at Harvard University is also gratefully acknowledged. Harvard-CNS is a member of the National Nanotechnology Infrastructure Network (NNIN). SM and CR were supported by DFG-Project RO1198/7-3 within the priority program SPP1125 nanowires.

References

[1] Huang M H, Mao S, Feick H, Yan H, Wu Y, Kind H, Weber E, Russo R and Yang P 2001 Room-temperature ultraviolet nanowire nanolasers *Science* **292** 1897–9

[2] Johnson J C, Yan H, Schaller R D, Haber L H, Saykally R J and Yang P 2001 Single nanowire lasers *J. Phys. Chem.* B **105** 11387–90

[3] Yu S F, Yuen C, Lau S P, Park W I and Yi G-C 2004 Random laser action in ZnO nanorod arrays embedded in ZnO epilayers *Appl. Phys. Lett.* **84** 3241–3

[4] Hsu H-C, Wu C-Y and Hsieh W-F 2005 Stimulated emission and lasing of random-growth oriented ZnO nanowires *J. Appl. Phys.* **97** 064315

[5] Han X, Wang G, Wang Q, Cao L, Liu R, Zou B and Hou J G 2005 Ultraviolet lasing and time-resolved photoluminescence of well-aligned ZnO nanorod arrays *Appl. Phys. Lett.* **86** 223106

[6] Johnson J C, Choi H-J, Knutsen K P, Schaller R D, Yang P and Saykally R J 2002 Single gallium nitride nanowire lasers *Nature Mater.* **1** 106–10

[7] Duan X, Huang Y, Agarwal R and Lieber C M 2003 Single-nanowire electrically driven lasers *Nature* **421** 241–5

[8] Agarwal R, Barrelet C J and Lieber C M 2005 Lasing in single cadmium sulfide nanowire optical cavities *Nano Lett.* **5** 917–20

[9] Chin A H, Vaddiraju S, Maslov A V, Ning C Z, Sunkara M K and Meyyappan M 2006 Near-infrared semiconductor subwavelength-wire lasers *Appl. Phys. Lett.* **88** 163115

[10] Siegman A E 1986 *Lasers* (Sausalito, CA: University Science Books)

[11] Zimmler M A, Bao J, Capasso F, Müller S and Ronning C 2008 Laser action in nanowires: observation of the transition from amplified spontaneous emission to laser oscillation *Appl. Phys. Lett.* **93** 051101

[12] Borchers C, Müller S, Stichtenoth D, Schwen D and Ronning C 2006 Catalyst-nanostructure interaction in the growth of 1-D ZnO nanostructures *J. Phys. Chem.* B **110** 1656–60

[13] Wang Z L (ed) 2005 *Nanowires and Nanobelts: Materials, Properties and Devices* (Berlin: Springer)

[14] Casperson L W 1975 Threshold characteristics of multimode laser oscillators *J. Appl. Phys.* **46** 5194–201

[15] Madelung O (ed) 2003 *Semiconductors: Data Handbook* (Berlin: Springer)

[16] Maslov A V and Ning C Z 2003 Reflection of guided modes in a semiconductor nanowire laser *Appl. Phys. Lett.* **83** 1237–9

[17] Yariv A 1997 *Optical Electronics in Modern Communications (Oxford Series in Electrical and Computer Engineering)* (Oxford: Oxford University Press)

[18] Voss T, Svacha G T, Mazur E, Muller S, Ronning C, Konjhodzic D and Marlow F 2007 High-order waveguide modes in ZnO nanowires *Nano Lett.* **7** 3675–80

[19] Sullivan D M 2000 *Electromagnetic Simulation Using the FDTD Method* (New York: Wiley)

[20] Bhattacharya P 1997 *Semiconductor Optoelectronic Devices* (Upper Saddle River, NJ: Prentice-Hall)

[21] Maslov A V and Ning C Z 2004 Modal gain in a semiconductor nanowire laser with anisotropic bandstructure *IEEE J. Quantum Electron.* **40** 1389–97

[22] Maslov A V and Ning C Z 2004 Far-field emission of a semiconductor nanowire laser *Opt. Lett.* **29** 572–4

[23] Landau L D, Lifshitz E M and Pitaevskii L P 1984 *Electrodynamics of Continuous Media* (Oxford: Butterworth-Heinenann)

[24] Chuang S L 1995 *Physics of Optoelectronic Devices* (New York: Wiley)

[25] Thomas D G and Hopfield J J 1962 Fluorescence in CdS and its possible use for an optical maser *J. Appl. Phys.* **33** 3243–9

[26] Haug H and Grob K 1967 Exciton laser theory *Phys. Lett.* A **26** 41–2

[27] Haug H 1968 Theory of laser action involving free excitons and LO-phonon-assisted transitions *J. Appl. Phys.* **39** 4687–95

[28] Haug H and Koch S 1977 On the theory of laser action in dense exciton systems *Phys. Status Solidi* b **82** 531–43

[29] Klingshirn C 1975 The luminescence of ZnO under high one- and two-quantum excitation *Phys. Status Solidi* b **71** 547–56
[30] Koch S W, Haug H, Schmieder G, Bohnert W and Klingshirn C 1978 Stimulated intrinsic recombination processes in II–VI compounds *Phys. Status Solidi* b **89** 431–40
[31] Wünstel W and Klingshirn C 1980 Tunable laser-emission from wurtzite-type II–VI compounds *Opt. Commun.* **32** 269–73
[32] Goto T and Langer D W 1971 Stimulated emission and excited states of the i_6 donor electron in ZnO *J. Appl. Phys.* **42** 5066–71
[33] Hvam J M 1974 Exciton interaction in photoluminescence from ZnO *Phys. Status Solidi* b **63** 511–7
[34] Park Y S and Schneider J R 1968 Index of refraction of ZnO *J. Appl. Phys.* **39** 3049–52
[35] Johnston W D Jr 1971 Characteristics of optically pumped platelet lasers of ZnO, CdS, CdSe, and $CdS_{0.6}Se_{0.4}$ between 300° and 80°K *J. Appl. Phys.* **42** 2731–40
[36] Packard J R, Campbell D A and Tait W C 1967 Evidence for indirect annihilation of free excitons in II–VI semiconductor lasers *J. Appl. Phys.* **38** 5255–7
[37] Hvam J M 1971 Temperature-induced wavelength shift of electron-beam-pumped lasers from CdSe, CdS, and ZnO *Phys. Rev.* B **4** 4459–64
[38] Nicoll F H 1966 Ultraviolet ZnO laser pumped by an electron beam *Appl. Phys. Lett.* **9** 13–5
[39] Jensen G Hvedstrup and Skettrup T 1973 Absorption edge and Urbach's rule in ZnO *Phys. Status Solidi* b **60** 169–73
[40] Leheny R F, Shaklee K L, Ippen E P, Nahory R E and Shay J L 1970 A new model for the temperature-dependent CdS laser *Appl. Phys. Lett.* **17** 494–7